Journal of Physical Chemistry C 122.28 (2018): 16389-16396

DOI: http://dx.doi.org/10.1021/acs.jpcc.8b03709

Compositional Tuning of Light-to-Heat Conversion Efficiency and of Optical Properties of Superparamagnetic Iron Oxide Nanoparticles

María Rivero[1], Jie Hu[2], Daniel Jaque[2], Magdalena Cañete[3], Jorge Sánchez-Marcos*[1], Alexandra Muñoz-Bonilla*[4]

[1] Synthesis and Electrochemical and Spectroscopic Characterization of Materials Group, Departamento de Química-Física Aplicada, Facultad de Ciencias, Universidad Autónoma de Madrid, C/Francisco Tomás y Valiente 7, 28049 Madrid, Spain.

[2] Fluorescence Imaging Group, Departamento de Física de Materiales, Facultad de Ciencias, Universidad Autónoma de Madrid, C/Francisco Tomás y Valiente 7, 28049 Madrid, Spain.

[3] Cell Biology Group, Departamento de Biología, Facultad de Ciencias, Universidad Autónoma de Madrid, C/Francisco Tomás y Valiente 7, 28049 Madrid, Spain.

[4] Macromolecular Engineering Group, Instituto de Ciencia y Tecnología de Polímeros (ICTP-CSIC), C/ Juan de la Cierva 3, 28006 Madrid, Spain

Email: jorge.sanchezm@uam (Jorge Sánchez-Marcos), sbonilla@ictp.csic.es (Alexandra Muñoz Bonilla)

Abstract

Superparamagnetic iron oxide nanoparticles have played a fundamental role in the recent development on nanomedicine, being one of the most popular imaging and therapeutic agents. Recently, the ability of iron magnetic nanoparticles for efficient heat generation under infrared optical excitation has even boosted the interest of scientific community in

this family of nanomaterials. Combination of magnetic and optical heating into a single nanostructure makes possible the development of advanced therapy treatments based on synergetic effects between these two heat sources that, in addition, could be combined with high penetration magnetic imaging. Despite of its potential, the application of iron oxide nanoparticles in photothermal treatments is limited because the lack of knowledge about the physical mechanisms behind their light-to-heat conversion capacity. In this work we have systematically investigated the photothermal efficiency of iron oxide nanoparticles with a variable composition achieved by partial replacement of iron by zinc atoms. We have experimentally found that the light-to-heat conversion efficiency gradually increases with the iron content, suggesting a dominant role of iron related transitions in the heating processes. Experimental data included in this work reveal a simple route to tailor the light activated heating processes in iron oxide nanoparticles towards fully controllable treatments.

1. Introduction

The beneficial effects of thermal therapy in the treatment of cancer have been recently demonstrated by many researches.[1] The controlled and localized increase of temperature leads to a large number of biological processes,[2] that are determined by both the temperature increment and the length of the treatment.[3] Moderate hyperthermia has demonstrated to improve the traditional treatments (such as chemotherapy or radiotherapy) when combined, reducing their negative side effects.[4] Severe hyperthermia (temperature increment above 10 °C applied for time periods of few minutes) have been demonstrated to provide effective *in vivo* tumor treatments.[5] Because of these results, the use and development of new nanomaterials for thermal therapy have attached the attention of the scientific community in the last few years, especially for magnetic hyperthermia treatments.[6] Nowadays, near-infrared (NIR) laser light irradiation based

photothermal treatments are appearing into scene as one of the most effective and non-invasive treatments.[7] For the achievement of efficient photothermal therapies (PTTs), nanomaterials to be used should show large light-to-heat conversion efficiencies. The use of excitation wavelengths lying in the NIR region (650-900 nm) is desirable for cancer therapies due to its minimal absorbance by water, while blood and tissue are maximally transmissive, allowing large (up to centimeters) penetration depths into tissues.[8] Many different types of photothermal therapy agents have been reported meeting those characteristics, being possible to combine them, creating smart multifunctional nanostructures for simultaneous diagnosis and therapy. Remarkable examples include gold[9-11] and copper sulfide[12,13] nanomaterials, carbon-based nanostructures as graphene oxide[14-16], carbon nanotubes[17] or carbon quantum dots[1819] and rare earth doped nanoparticles[20-22]. Recently, the use of magnetic materials such as superparamagnetic iron oxide nanoparticles (SPIONs) in PTTs has emerged as interesting alternative.[23-26] In addition to their recently demonstrated light-to-heat conversion ability, SPIONs exhibit low toxicity and biocompatibility, easy functionalization and excellent magnetic properties which allow magnetic targeting.[27] SPIONS are also inherent contrast agents for magnetic resonance imaging (MRI) and by the incorporation of additional components can enable complementary imaging modalities.[28] Thus, investigation of the photothermal behavior of SPIONs has become an interesting topic for research community and has attracted a great attention in recent years. Sadat *et al.* and Zhao *et al*. identified the mechanism of the photothermal effect of Fe_3O_4 NPs in terms of photoluminiscense emission in the NIR region.[29,30] However, despite the large number works published, the mechanisms that govern this phenomenon are still far from being fully understood.

Most researches are focused in ferrites nanoparticles (NPs), which are the typically employed for biomedical applications. Ferrites have a general formula $(M_{1-\alpha}Fe_{\alpha})[M_{\alpha}Fe_{2-\alpha}]O_4$, where M corresponds to a divalent cation (M = Fe, Co, Ni, Mn, Zn), and ( ) and [ ] represent tetrahedral and octahedral cation sites, respectively, in a face-centered cubic oxygen anion sublattice. The inversion degree, α, denotes de cation distribution in the spinel structure.[31] Magnetic properties of the ferrite NPs are determined by the cation substitution and distribution in the spinel structure as well as others as well as others as particle size and shape).[32]

Herein, we design superparamagnetic zinc doped iron oxide ferrite NPs for PTT with variable zinc content in the structure $Zn_xFe_{3-x}O_4$ ($0 < x < 1$). The influence of the divalent cation percentage in the ferrite NPs on heating efficiency (Φ_{heat}) is systematically investigated. The NPs were synthesized by an electrochemical method that allows controlling the chemical composition of the NPs, maintaining similar particle diameter. This allows to study exclusively the effect of the divalent cation content on the Φ_{heat}, avoiding particle size contribution, which could shed some light on mechanism of photothermal effect in magnetic NPs. The relation between Φ_{heat} and NPs composition is discussed in terms of the composition induced variation of their optical properties.

2. Experimental Section

2.1. Materials

A series of zinc ferrites NPs with variable composition, $Zn_xFe_{(3-x)}O_4$ (x = 0.2, 0.5, 0.8) and a particle size of ~12 nm were synthesized following an electrochemical method in aqueous medium as previously described.[33,34] Dopamine hydrochloride, *N*-(3-dimethylaminopropyl)-*N*′-ethylcarbodiimide (EDC), *N*-hydroxysuccinimide (NHS), citric acid, ethanol (EtOH) and acetonitrile (ACN) were provided by Sigma-Aldrich and

used without further purification. The cell viability study was performed with cell cultures from cervical adenocarcinoma human uterus, HeLa cells (ATCC® CCL2™, LGC Standards S.L.U., Manassas, VA, USA) and analyzed with 3-(4,5-dimethylthiazol-2-yl)-2,5-diphenyl-2H tetrazolium bromide (MTT) purchased from Sigma-Aldrich.

2.2. Surface modification of zinc ferrites NPs

The surface of the zinc ferrite NPs was first modified with dopamine (DA) molecules ($Zn_xFe_{(3-x)}O_4$@DA NPs). DA was attached to the NPs surface via catechol chemistry, obtaining an active NPs surface with free amino groups for post-functionalization processes.[35] For that purpose, 20 mg of ferrite NPs were dispersed in 3 mL of ACN and 250 mg of dopamine hydrochloride were added to the solution. The mixture was treated in an ultrasonic bath for 1 hour. The resultant solution was centrifuged and washed repeatedly with EtOH/distilled water and stored in the fridge. Then, the $Zn_xFe_{(3-x)}O_4$@DA NPs were further functionalized with citric acid. In brief, citric acid molecules were linked to the amino groups of the NPs surface via ethyl-3-(3-dimethylaminopropyl)-carbodiimide/N-hydroxysuccinimide (EDC/NHS) mediated coupling reaction. Citric acid (0.16 mmol) was first dissolved in a volume of 10 mL of DMF/distilled water (1:1), at pH 8. Then, 0.32 mmol of EDC and NHS were added to the solution. The pH was readjusted to 8 and the mixture was left 4 h under magnetic stirring and dark conditions for the citric acid molecules activation reaction. Finally, the $Zn_xFe_{(3-x)}O_4$@DA NPs aqueous suspension was added drop by drop to the mixture and kept stirring for 12 h in dark conditions for the conjugation reaction. Afterwards, the $Zn_xFe_{(3-x)}O_4$@Citric NPs were thoroughly washed with distilled water.

2.3. Characterization

The stoichiometry of the zinc ferrite NPs was determined by chemical analysis of the synthesized material, performed through inductively coupled plasma optical emission spectroscopy (ICP-OES) using a Perkin Elmer Optima 2100 DV system. The crystalline structure was studied by X-ray diffraction (XRD). The X-ray diffractograms were recorded between 5º and 80º 2θ in a X'Pert PRO Theta/2Theta diffractometer, equipped with a SOL-X Bruker detector with Cu Kα radiation and analyzed using the FullProf Suite[36] program based on the Rietveld method.[37] Transmission electron microscopy (TEM) images of the samples were recorded in a JEOL JEM 1010 operating at acceleration voltage of 100 kV, to determine the particle size and morphology of the NPs. The extinction spectra were recorded with a UV-Vis spectrophotometer (Perkin Elmer Lambda 35). The magnetic properties were analyzed with a Vibrating Sample Magnetometer (VSM) MLVSM9 MagLab 9T, Oxford Instruments with a saturating field of 1 T. Thermogravimetric analysis (TGA) was performed to determine the percentage of organic coating using a TA Instrument (DSC/DTA/TGA Q600 model) with a heating rate of 10 ºC min^{-1}, starting at room temperature up to 800 ºC under dynamic air atmosphere. Fourier transform infrared spectroscopy (FTIR) measurements were carried out on a Bruker IFS66v using KBr pellets to analyze the coating of the NPs. The colloidal stabilities of the NPs were analyzed in a Zetasizer Nano S, from Malvern Instruments (UK). The hydrodynamic size was determined by dynamic light scattering (DLS) and the ζ- Potential was measured as a function of pH at 25 °C, using HNO_3 and KOH to adjust the pH of the suspensions.

2.4. NIR photothermal heating effect

The photothermal effect of the $Zn_xFe_{(3-x)}O_4$@Citric (x = 0.2, 0.5, 0.8) NPs induced by NIR laser irradiation was evaluated by exposing NPs aqueous suspensions (0.5 mL, 0.25 mg mL^{-1}) at room temperature to an 800 nm laser with variable power density (0.6, 0.8,

1.1 and 1.4 W cm^{-2}). The samples were irradiated for 10 min (LASER ON), following by naturally cooling to room temperature without NIR laser irradiation (LASER OFF). The time evolution of NPs suspensions' temperature was monitored with a FLIR E40 thermal camera.

2.5. Dark field microscopy.

In order to determine the effect that chemical composition has on the optical properties of the here studied $Zn_xFe_{(3-x)}O_4$ NPs, dark field microscopy experiments were also conducted. $Zn_xFe_{(3-x)}O_4$ NPs were deposited on a microscope cover slip by letting a droplet of colloidal solution dry. Once the liquid medium had become completely evaporated, the sample was imaged in a microscope equipped with a dark-field condensed (NA 0.8) and a 50X microscope objective with a numerical aperture of 0.65. The compositional dependence of the scattering efficiency of the $Zn_xFe_{(3-x)}O_4$ NPs in the visible range was then qualitatively estimated by determining the averaged scattered light intensity per single NP.

2.6. Cell cultures and viability studies

Hela cells were cultivated in a 200 SteriCult (Hucoa-Erlöss, Thermo Fisher) incubator at 37 °C and 5% CO_2 atmosphere in DMEM (Dulbecco's modified Eagle's medium) supplemented with 10% FBS v/v (fetal bovine serum) and 5% v/v penicillin/streptomycin. All products were obtained from Invitrogen (Paisley, UK). Cells were seeded in multi-well plates from Corning Inc. (New York, NY, USA), and incubated over 24 h with various concentrations of magnetic NPs from 0.01 to 0.5 mg mL^{-1}. Then, the medium was removed, and the cells, after washing step, were incubated with MTT PBS solution to a final concentration of 0.05 mg mL^{-1}. After 3 h of incubation, the medium was eliminated and reduced formazan was dissolved in 500 μL of DMSO per

well and was measured as absorbance at 540 nm in a SpectraFluor spectrophotometer (Tecan, Switzerland). Cell survival was expressed as the percentage of absorption of treated cells in comparison with control cells. Data corresponded to mean values ± standard deviation from at least three different experiments.

In order to evaluate the NP uptake, HeLa cells were grown on coverslips and incubated 24 h in the same experimental conditions as in the MTT assay. Then, the cells were washed three times with PBS and fixed with cold methanol during 5 min, stained with toluidine blue (TB, 0.05 mg/mL distilled water) for 1 min, washed with distilled water and air-dried. The preparations were mounted on DePeX (Serva) and observed under bright field microscopy in an Olympus BX61 epifluorescence microscope, equipped with an Olympus DP50 digital camera Micromax (Princeton Instruments).

3. Results and Discussion

3.1. NPs synthesis and characterization

The synthesis of zinc ferrite NPs with controlled size and composition was carried out following a single-step electrochemical method previously described.[33,34] By this method, different NPs were prepared with variable zinc content in their structure but maintaining similar diameters, by simply varying the temperature of reaction and the current intensity applied during the electrochemical synthesis. This is remarkably because typically, a variation of the chemical composition conducts to a change in the particle size,[38] which makes difficult to investigating the influence of each parameter on the NPs properties. In this work, we exclusively study the effect of the chemical composition on the photothermal behavior without any additional contribution due to variation on the particle size. The stoichiometry of the NPs determined by the ICP-OES analysis was found to be $Zn_{0.2}Fe_{2.8}O_4$, $Zn_{0.5}Fe_{2.5}O_4$ and $Zn_{0.8}Fe_{2.2}O_4$, while the X-ray diffraction refinements

confirm a similar crystal size for all the composition, ~12 nm (Table 1). The X-ray diffractograms (Figure 1) also confirm for all the samples the presence of a pure single crystalline phase, where all peaks can be indexed according to the Fd-3m: 227 cubic spinel structures.

Table 1. Sample stoichiometry determined by ICP-OES, particle sizes obtained by TEM and crystal sizes estimated by Rietveld refinement of the X-ray diffractograms.

Sample	Particle size (nm)	Crystal size (nm)
$Zn_{0.2}Fe_{2.8}O_4$	12 ± 3	11 ± 1
$Zn_{0.5}Fe_{2.5}O_4$	11 ± 2	12 ± 1
$Zn_{0.8}Fe_{2.2}O_4$	11 ± 2	12 ± 1

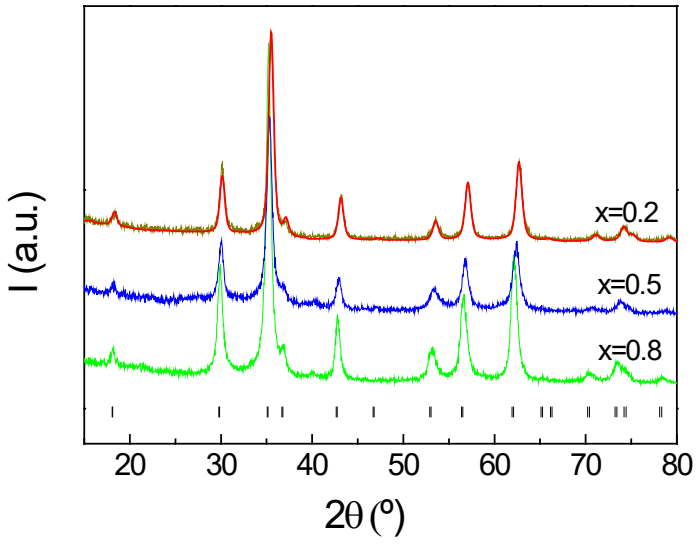

Figure 1. X-ray diffraction patterns of the $Zn_xFe_{(3-x)}O_4$ (x = 0.2, 0.5, 0.8) NPs with different composition and similar size. Bragg positions are marked (I). The sample x = 0.2 shows the excellent Rietveld refinement in a red line.

The TEM micrographs show a quasi-spherical shape of the NPs and an adequate aggregation degree. Figure 2a displays as an example the image of sample $Zn_{0.2}Fe_{2.8}O_4$ with its size polydispersity (Figure 2b) calculated by measuring at least 100 NPs. For all the samples values close to 12 nm of diameter were obtained, with an acceptable polydispersity degree. Both crystal and particles sizes are in good agreement (Table 1), pointing out the monocrystalline character of the NPs.

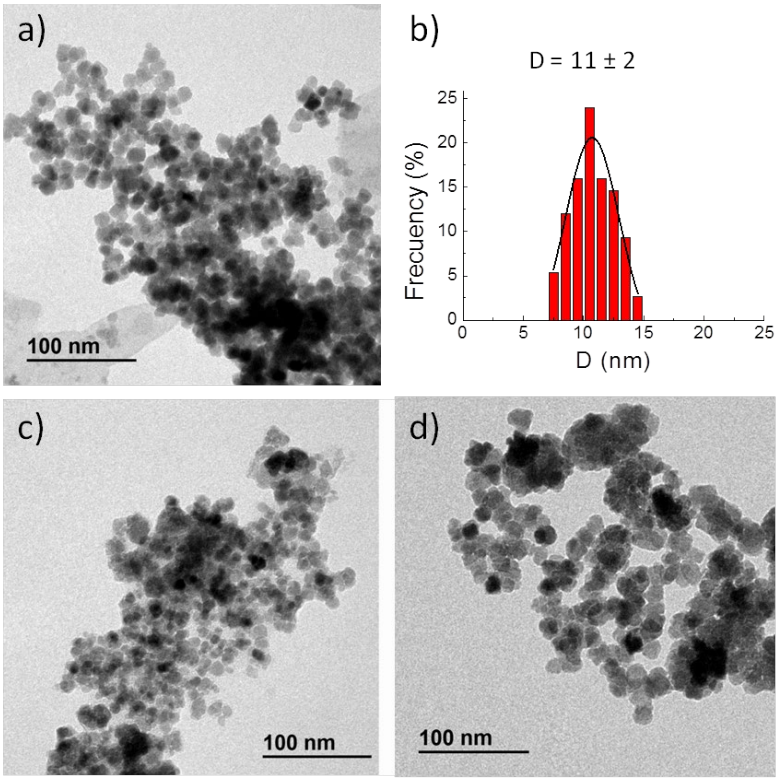

Figure 2. TEM micrographs of (a) $Zn_{0.2}Fe_{2.8}O_4$ NPs with (b) its particle size distribution, (c) $Zn_{0.2}Fe_{2.8}O_4$@DA NPs and (d) $Zn_{0.2}Fe_{2.8}O_4$@Citric NPs.

As it was mentioned before, the magnetic properties of the spinel ferrites are determined by the composition, which is influenced by the synthesis method. Figure 3a contains the magnetic characterization of the three NPs compositions, $Zn_xFe_{(3-x)}O_4$ (x = 0.2, 0.5, 0.8), in which is clearly observed that the magnetic saturation values (M_S) decreases with the increment of Zn in the crystalline structure.[39] Thus, the magnetic properties can be easily

tuned by controlling the Zn content. Remarkably, all the samples present superparamagnetic behavior at 290 K, making them suitable for controlled magnetic manipulation.

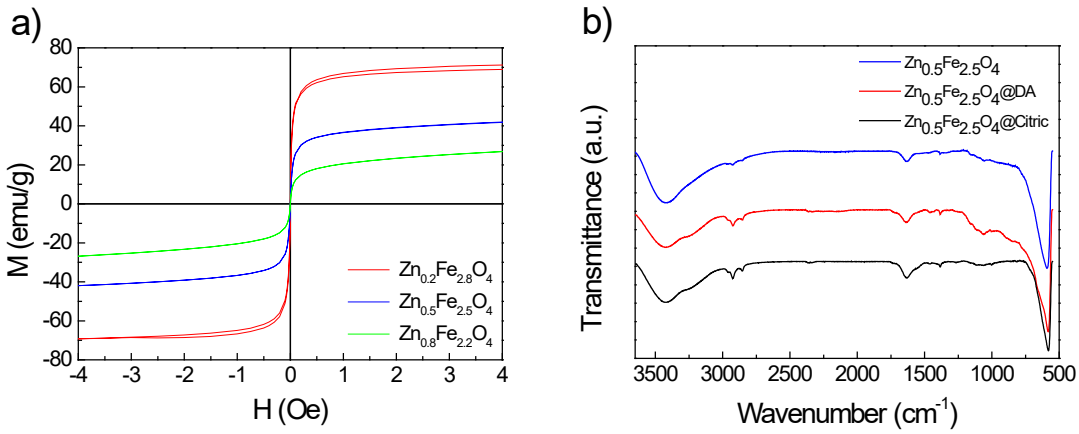

Figure 3. a) Magnetic hysteresis loops *M–H* measured at 290 K for $Zn_{0.2}Fe_{2.8}O_4$@Citric, $Zn_{0.5}Fe_{2.5}O_4$@Citric, $Zn_{0.8}Fe_{2.2}O_4$@Citric NPs. b) FTIR spectra of $Zn_{0.5}Fe_{2.5}O_4$, $Zn_{0.5}Fe_{2.5}O_4$@DA and $Zn_{0.5}Fe_{2.5}O_4$@Citric NPs.

As commented, the ferrite NPs were surface functionalized following a covalent approach based on the formation of stable linker between hydroxyl groups on the NPs surface and DA as anchoring agent.[35,39] Then, the free amine groups of DA attached on the surface allows for post-functionalization of the coated magnetic particles with other functional molecules.[40] In this work, we used citric acid as functional group to stabilize the magnetic NPs in aqueous solution. The Figure 3b shows as an example the FTIR spectrum of the $Zn_{0.5}Fe_{2.5}O_4$ NPs coated with citric acid, $Zn_{0.5}Fe_{2.5}O_4$@Citric, in comparison with the spectra of the uncoated NPs and $Zn_{0.5}Fe_{2.5}O_4$@DA sample, that provides evidence of organic coating. The spectrum of the DA coated NPs shows additional bands with respect to $Zn_{0.5}Fe_{2.5}O_4$ NPs, due to the vibration modes of dopamine molecules such as the C–H vibrations between ~2970-2850 cm^{-1}, the NH stretching at ~3250 cm^{-1} and benzene ring C-C vibration at ~1450 cm^{-1}. The spectrum of the NPs after the attachment of the citric

acid exhibit a band at at ~1725 cm^{-1} ascribed to the C=O of the citric acid. The loading amount of the organic layer attached onto the NPs surface was measured by thermogravimetric analysis (TGA). The percentages of weight losses due to the combustion of the organic material are summarized in Table 2. All the values are similar, around 10 %, pointing out that the organic layer has a similar thickness in all the samples.

In the TEM micrographs of the surface functionalized NPs (Figure 2c and 2d) it can be seen that they maintain a similar size and shape, suggesting that the coating process is not harmful for the material. This fact was corroborated by the ICP-OES analysis of the coated samples, which indicates that the NPs still maintain the selected stoichiometry.

3.2. Colloidal characterization

The surface functionalization with citric acid provides colloidal stability due to the steric and electrostatic repulsions to the NPs, which were stable in aqueous solutions for at least one month. The colloidal properties of the NPs solutions were further evaluated by ζ-Potential and hydrodynamic diameter measurements, at pH 7 (Table 2). The ζ-Potential values summarized in Table 2, indicate high negative charges due to the presence of the carboxylic groups of the citric acid molecules, which demonstrate the success of the surface functionalization. In addition, the values are well above ±35 mV enough for the NPs to repel each others, giving rise to stable colloidal dispersions.[41]

Table 2. Organic coating percentage determined by TGA and colloidal properties including hydrodynamic size (D_H), PDI (polydispersity index) and ζ-Potential values of the aqueous suspension of surface coated NPs at pH 7.

Sample	Organic coating (%)	D_H (nm)	PDI	ζ-Potential (mV)

$Zn_{0.2}Fe_{2.8}O_4$@Citric	9	198	0.210	-46 ± 4
$Zn_{0.5}Fe_{2.5}O_4$@Citric	10	187	0.243	-44 ± 3
$Zn_{0.8}Fe_{2.2}O_4$@Citric	8	196	0.180	-40 ± 4

3.3. NIR photothermal heating effect

The three NPs compositions were firstly investigated by UV-Vis spectroscopy, showing an effective optical extinction in the visible and NIR regions (Figure 4a). From a first inspection of Figure 4a, it seems that the extinction coefficient tends to decrease as the amount of zinc in the sample is increased. Figure 4b shows the increase in the temperature of aqueous solutions of 0.25 mg mL^{-1} $Zn_xFe_{3-x}O_4$@Citric (X = 0.2, 0.5, 0.8) under a 1.4 W cm^{-2} power density, for 10 min of irradiation. In all cases, the temperature of the aqueous solutions rapidly increases during laser irradiation, reaching a steady value at around 5 minutes. A non-representative temperature increase is observed for the control of distilled water. As it could be expected from the UV-Vis spectroscopy results, there is an evident influence of the chemical composition in the heating response of the NPs, increasing the efficiency as the amount of zinc decreases in the sample. The temperature of the suspension containing $Zn_{0.8}Fe_{2.2}O_4$@Citric NPs was raised 5.8 ºC, the suspension of $Zn_{0.5}Fe_{2.5}O_4$@Citric raised 10 ºC and finally, the $Zn_{0.2}Fe_{2.8}O_4$@Citric suspension was heated up to 11 ºC. Therefore, these results confirm that the ferrite NPs can effectively absorb the 800 nm laser energy and convert it into heat, and the NPs containing low content of Zn were more efficient in inducing a temperature increase with the same concentration, power density and exposure time.

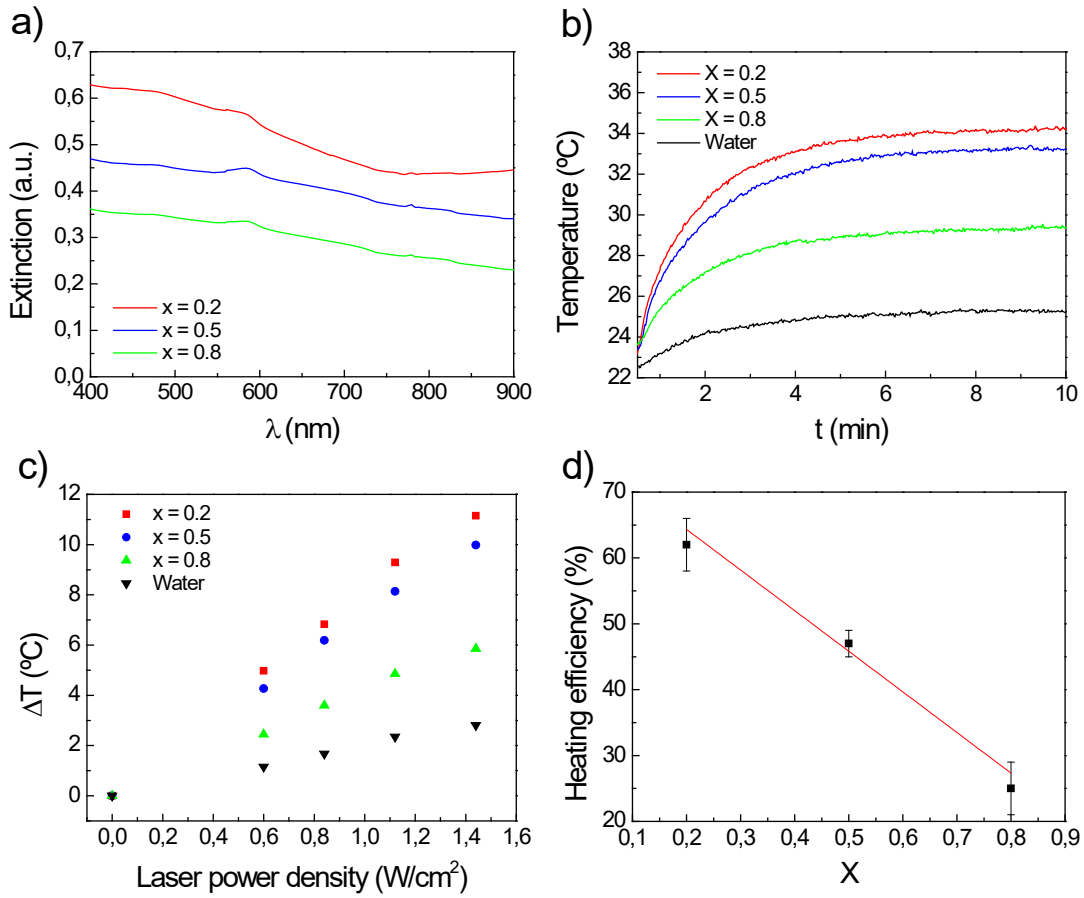

Figure 4. Heating response analysis of $Zn_xFe_{3-x}O_4$@Citric (x = 0.2, 0.5, 0.8) NPs. a) UV-vis extinction spectra of the NPs dispersed in distilled water (0.25 mg mL^{-1}); b) temperature increase in aqueous suspension at 0.25 mg mL^{-1} of NPs under a 1.4 Wcm^{-2} power irradiation and c) under variable laser power irradiation; d) heating efficiencies.

The photothermal conversion efficiency (ŋ) of the four samples was calculated from the cooling rate, according to equation 1[38]:

$$\eta = \frac{hA\,(T_{max} - T_o) - Q_o}{I\,(1 - 10^{-OD})} \qquad (1)$$

where h is the heat transfer coefficient, A is the sample well surface area, T_{max} is the maximum temperature of the solution after laser irradiation, T_o is the ambient temperature, Q_o is the energy dissipated from light absorbed by the solvent (distilled

water), *I* is the incident laser power and *OD* is the optical density of the sample solution at 808 nm. The value of *hA* is derived according to equation 2:[42]

$$\tau_S = \frac{m_S - C_S}{hA} \quad (2)$$

where τ_s is the sample system time constant, m_s is the mass and C_s is the heat capacity of distilled water used as solvent.

According to equation 1, the photothermal conversion efficiencies were determined to be 62 % for $Zn_{0.2}Fe_{2.8}O_4$@Citric sample, 47 % for $Zn_{0.5}Fe_{2.5}O_4$@Citric sample and 25 % for $Zn_{0.8}Fe_{2.2}O_4$@Citric sample. It is worth noting that these obtained values are significantly high comparing with those previously reported for other ferrites with similar sizes,[4, 43] or other combined magnetic systems.[44-47] This improved efficiency would allow for the use of reduced concentration and NIR irradiation doses in future photothermal treatments. This indeed, makes these NPs excellent candidates in NIR photothermal therapy, using them alone or combining them in multifunctional systems. Furthermore, it has been found that ŋ varies linearly with the zinc doping level, making possible the design of magnetic NPs with desired photothermal conversion properties (Figure 4d) by varying the chemical composition. To the best of our knowledge, this is the first study in which the influence of the transition metal dopant in ferrites NPs on the photothermal efficiency was investigated. Results here reporting on the possible tuning of the optical heating efficiency of magnetic NPs are, indeed, in accordance with recent results that also showed how this heating efficiency can be greatly tuned by controlled modifications of either their surface coating or size.[29]

Results included in Figure 4d clearly reveal that compositional tuning of ferrite NPs towards a less metallic character significantly reduces the heating efficiency of the structure. Indeed, experimental data seem to indicate that complete replacement of Fe by

Zn ions would lead to an almost vanished light-to-heat conversion efficiency. The exact origin of this reduction, as well as of the mechanism, leading to light induced heating by ferrite NPs, is not well understood at present time. Nevertheless, our experimental data suggest that this strongly related to the iron content and, thus, that this is correlated to the absorption of IR light by Fe and the subsequent relaxation by non-radioactive transitions. Independently to the physical mechanism behind, experimental data included in Figure 4d demonstrate the potential tailoring of heating efficiency of ferrite NPs by simple compositional tuning.

The possibility of tuning the intrinsic optical properties of $Zn_xFe_{3-x}O_4$ NPs has been also evaluated by performing dark field experiments.

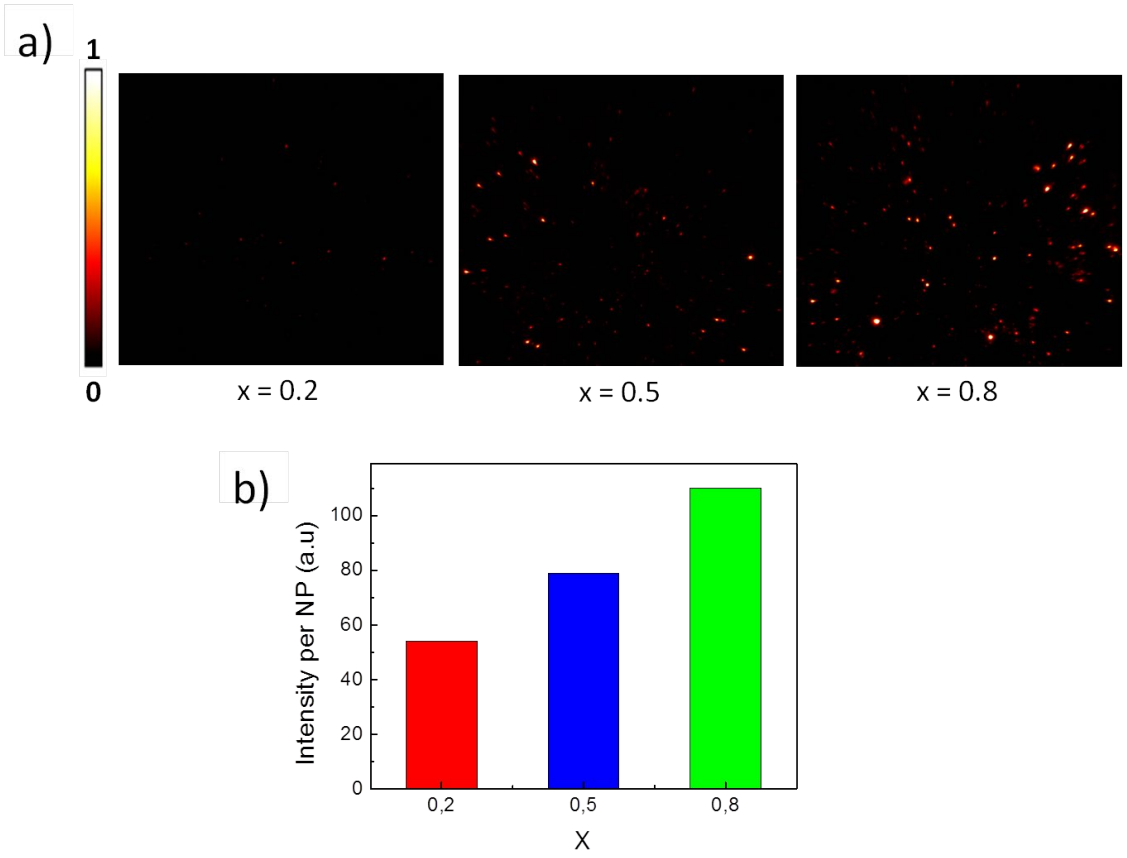

Figure 5. a) Dark field images and b) intensity per NPs of $Zn_xFe_{3-x}O_4$@Citric (x = 0.2, 0.5, 0.8) NPs.

Figure 5 includes the dark field images obtained for the three compositions studied in this work. The contrast in dark-field microscopy images is proportional to the scattering efficiency of single NPs. It is evident how the dark-field contrast is significantly improved as the Zn content is increased. This is even more evident in Figure 5b where the averaged scattered intensity per NP is plotted for the different Zn contents. This unequivocally indicates that the scattering cross section per NP increases with the Zn content. This result, in combination with the decrease in the photothermal conversion efficiency with the Zn content suggest that as the Zn content is increased the scattering efficiency is increased at a expenses of the absorption (photothermal) efficiency. Again, the strong relation between the optical (scattering, absorption, extinction) properties of Fe-based magnetic NPs and their single particle characteristics is not new. M.E. Sadat already reported on a strong influence on particle size and coating on the balance between scattering and absorption cross sections in Fe_3O_4 NPs.[29]

These results evidence the possibility of tailoring the intrinsic optical properties and photothermal efficiency of $Zn_xFe_{3-x}O_4$ NPs, which could be very useful in theranostics applications, in which the nanoparticles can maintain the imaging performance under irradiation, controlling at the same time its heat capacity for minimal injury to normal tissues.

3.4. NPs internalization and cell viability

To ensure the possible use of the zinc ferrite NPs in photothermal therapies, *in vitro* studies were carried out in the human cervical carcinoma HeLa cell line, to determine the toxicity and the effective internalization of the NPs in the cells.

Figure 6 shows the cell viability (%) obtained by the MTT assay,[48] after 24 h of cell incubation with the $Zn_{0.5}Fe_{2.5}O_4$@Citric NPs at different concentrations up to 0.5 mg mL^{-}

[1]. The results revealed that viability of the cell culture was not significantly reduced as a result of the NPs exposition under all the experimental conditions.

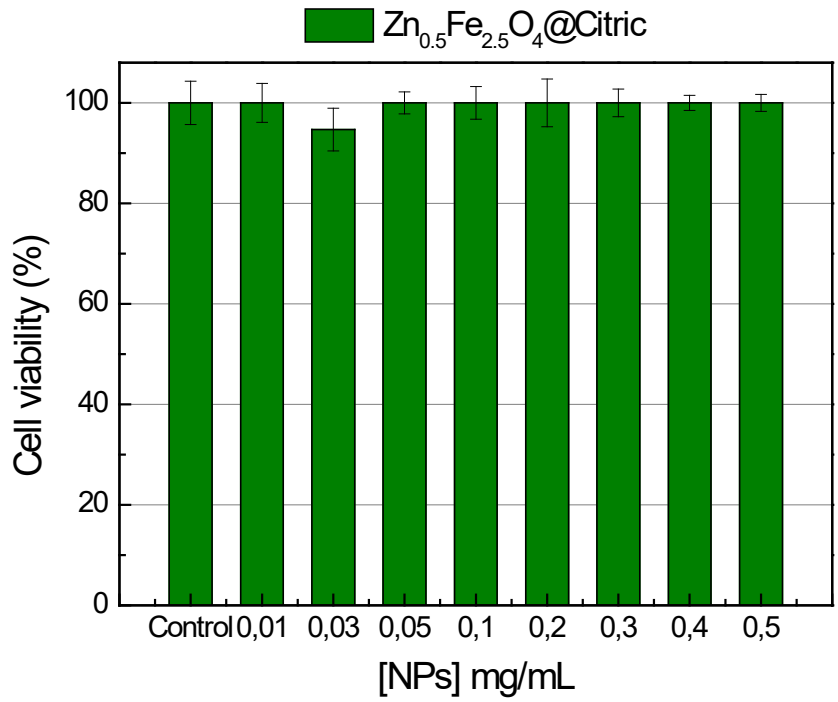

Figure 6. Evaluation of cell viability by MTT assay in the HeLa cell line, after 24 h of exposition to the $Zn_{0.5}Fe_{2.5}O_4$@Citric NPs at different concentrations. Data represent means ± SD (n = 3).

To evaluate the NPs cell internalization, the HeLa cells were exposed to $Zn_{0.5}Fe_{2.5}O_4$@Citric NPs in the same experimental conditions as the MTT assay. For the cell visualization, they were stained by the toluidine blue method. Figure 7 shows the untreated cells used as a control (a) and the exposed cells to 0.1 mg mL^{-1} (b), 0.3 mg mL^{-1} (c) and 0.5 mg mL^{-1} (d). It can be clearly seen the evident accumulation of NPs inside the cells, in particular in the cytoplasmic area, being this proportional to the concentration used. The cell morphology remains similar to that of control cells in all cases, corroborating the absence of toxicity in the range of concentrations. These results are in concordance with the previous MTT assay results.

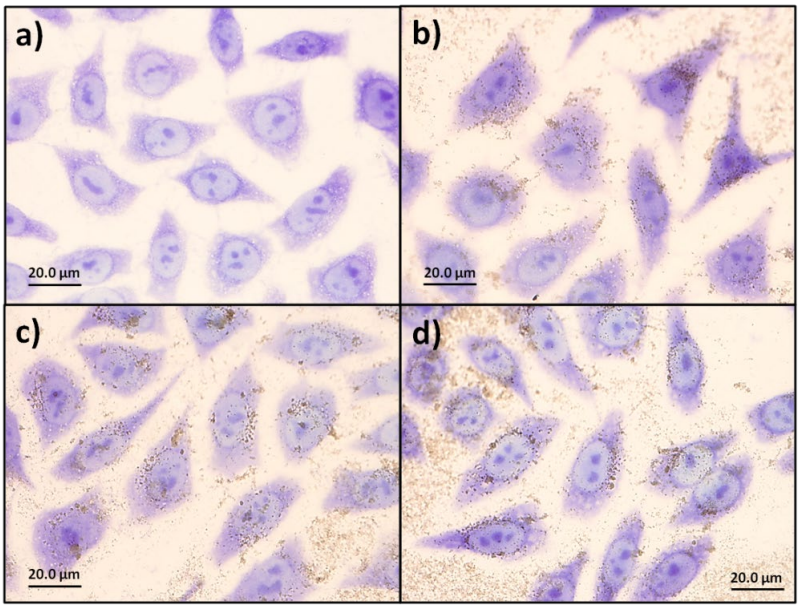

Figure 7. Internalization of $Zn_{0.5}Fe_{2.5}O_4$@Citric in HeLa cells at different concentrations: a) control, b) 0.1 mg mL^{-1} c) 0.3 mg mL^{-1} y d) 0.5 mg mL^{-1} of NPs.

4. Conclusions

Superparamagnetic zinc ferrite NPs with different composition, $Zn_xFe_{3-x}O_4$ (x = 0.2, 0.5, 0.8) and similar size, 12 nm, were synthesized by an electrochemical method. Their optical (extinction, scattering and absorption) properties have been systematically investigated. Experimental data revealed that chemical composition plays a key role in determining the optical properties of magnetic NPs. It is here demonstrated that a reduction in the Zn content leads to a simultaneous decrease in the photothermal efficiency and to an enhancement in the scattering cross section. It is, therefore, possible to pre-tailor the light induced heating and optical properties of magnetic properties during synthesis procedure. This possibility, together with their potential surface decoration makes $Zn_xFe_{3-x}O_4$ NPs excellent candidates for its employment in magneto-photothermal theranostics, using them either as a single entity or in multifunctional combined systems. The *in vitro* experiments in HeLa cells evidence de low toxicity of the material.

Acknowledgment

This work was supported financially by the MINECO (Projects MAT2015-67557-C2-2-P, CTQ2016-78454-C2-2-R and MAT2016-75362-C3-1-R), the Agencia Estatal de Investigación (AEI, Spain), Fondo Europeo de Desarrollo Regional (FEDER, EU), the Instituto de Salud Carlos III (PI16/00812), by Comunidad Autónoma de Madrid (B2017/BMD-3867RENIM-CM) and by the European Comission (NanoTBTech). This work has been also partially supported by COST action CM1403. J. H. acknowledges the scholarship from the China Scholarship Council (No. 20150665003).

References

(1) Mallory, M.; Gogineni, E.; Jones, G. C.; Greer, L.; Simone. C. B. Therapeutic Hyperthermia: the Old, the New, and the Upcoming. *Crit. Rev. Oncol. Hematol.* **2016**, *97*, 56–64.

(2) Hildebrandt, B.; Wust, P.; Ahlers, O.; Dieing, A.; Sreenivasa, G.; Kerner, T.; Felix, R.; Riess, H. The Cellular and Molecular Basis of Hyperthermia. *Crit. Rev. Oncol. Hematol.* **2002**, *43*, 33–56.

(3) Melancon, M. P.; Zhou, M.; Li, C. Cancer Theranostics with Near-Infrared Light-Activatable Multimodal Nanoparticles. *Acc. Chem. Res.* **2011**, *44*, 947–956.

(4) Oh, Y.; Je, J. Y.; Moorthy, M. S.; Seo, H.; Cho, W. H. pH and NIR-Light-Responsive Magnetic Iron Oxide Nanoparticles for Mitochondria-Mediated Apoptotic Cell Death Induced by Chemo-Photothermal Therapy. *Int. J. Pharm.* **2017**, *531*, 1–13.

(5) Benyettou, F.; Ocadiz Flores, J. A.; Ravaux, F.; Rezgui, R.; Jouiad, M.; Nehme, S. I.; Parsapur, R. K.; Olsen, J.-C.; Selvam, P.; Trabolsi, A. Mesoporous γ-Iron Oxide

Nanoparticles for Magnetically Triggered Release of Doxorubicin and Hyperthermia Treatment. *Chem. - A Eur. J.* **2016**, *22*, 17020–17028.

(6) Abenojar, E. C.; Wickramasinghe, S.; Bas-Concepcion, J.; Samia, A. C. S. Structural Effects on the Magnetic Hyperthermia Properties of Iron Oxide Nanoparticles. *Prog. Nat. Sci. Mater. Int.* **2016**, *26*, 440–448.

(7) Jaque, D.; Martínez Maestro, L.; del Rosal, B.; Haro-Gonzalez, P.; Benayas, A.; Plaza, J. L.; Martín Rodríguez, E; García Solé, J. Nanoparticles for Photothermal Therapies. *Nanoscale* **2014**, *6*, 9494-9530.

(8) Gobin, A. M.; Lee, M. H.; Halas, N. J.; James, W. D.; Drezek, R. A.; West, J. L. Near-Infrared Resonant Nanoshells for Combined Optical Imaging and Photothermal Cancer Therapy. *Nano Lett.* **2007**, *7*, 1929– 1934.

(9) Abadeer, N. S.; Murphy. C. J. Recent Progress in Cancer Thermal Therapy Using Gold Nanoparticles. *J. Phys. Chem. C* **2016**, *120*, 4691-4716.

(10) Kennedy, L. C.; Bickford, L. R.; Lewinski, N. A.; Coughlin, A. J.; Hu, Y.; Day, E. S.; West, J. L.; Drezek, R. A. A New Era for Cancer Treatment: Gold-Nanoparticle-Mediated Thermal Therapies. *Small* **2011**, *7*, 169–183.

(11) Yang, Y.; Lin, Y.; Di, D.; Zhang, X.; Wang, D.; Zhao, Q.; Wang, S. Gold Nanoparticle-Gated Mesoporous Silica as Redox-Triggered Drug Delivery for Chemo-Photothermal Synergistic Therapy. *J. Colloid Interface Sci.* **2017**, *508*, 323–331.

(12) Wang, S.; Riedinger, A.; Li, H.; Fu, C.; Liu, H.; Li, L.; Liu, T.; Tan, L.; Barthel, M. J.; Pugliese, G.; et al. Plasmonic Copper Sulfide Nanocrystals Exhibiting Near-Infrared Photothermal and Photodynamic Therapeutic Effects. *ACS Nano* **2015**, *9*, 1788–1800.

(13) Guo, L.; Yan, D. D.; Yang, D.; Li, Y.; Wang, X.; Zalewski, O.; Yan, B.; Lu, W. Combinatorial Photothermal and Immuno Cancer Therapy Using Chitosan-Coated Hollow Copper Sulfide Nanoparticles. *ACS Nano* **2014**, *8*, 5670–5681.

(14) Robinson, J. T.; Tabakman, S. M.; Liang, Y.; Wang, H.; Casalongue, H. S.; Vinh, D. Dai, H. Ultrasmall Reduced Graphene Oxide with High Near-Infrared Absorbance for Photothermal Therapy. *J. Am. Chem. Soc.* **2011**, *133*, 6825–6831.

(15) Tian, B.; Wang, C.; Zhang, S.; Feng, L.; Liu, Z. Photothermally Enhanced Photodynamic Therapy Delivered by Nano-Graphene Oxide. *ACS Nano* **2011**, *5*, 7000–7009.

(16) Otari, S. V.; Kumar, M.; Anwar, M. Z.; Thorat, N. D.; Sanjay, K.; Patel, S.; Lee, D.; Lee, J. H.; Lee, J.; Kang, Y. C. et al. Rapid Synthesis and Decoration of Reduced Graphene Oxide with Gold Nanoparticles by Thermostable Peptides for Memory Device and Photothermal Applications. *Sci. Rep.* **2017**, *7*, 10980.

(17) Zhang, M.; Wang, W.; Wu F.; Yuan, P.; Chi, C. Magnetic and Fluorescent Carbon Nanotubes for Dual Modal Imaging and Photothermal and Chemo-Therapy of Cancer Cells in Living Mice. *Carbon* **2017**, *123*, 70–83.

(18) Bao, Y.-W.; Hua, X.-W.; Li, Y.-H.; Jia, H.-R.; Wu, F.-G. Hyperthemia-Promoted Cytosolic and Nuclear Delivery of Copper/Carbon Quantum Dot-Crosslinked Nanosheets: Multimodal Imaging-Guided Photothermal Cancer Therapy. *ACS Appl. Mater. Interfaces*, **2018**, *10*, 1544-1555.

(19) Hassan, M.; Gomes, V. G.; Dehghani, A.; Ardekani, S. M. Engineering Carbon Quantum Dots for Photomediated Theranostics. *Nano Res.* **2018**, *11*, 1–41.

(20) Lv, R.; Zhong, C.; Li, R.; Yang, P.; He, F.; Gai, S.; Hou, Z.; Yang, G.; Lin, J. Multifunctional Anticancer Platform for Multimodal Imaging and Visible Light Driven Photodynamic/Photothermal Therapy. *Chem. Mater.* **2015**, *27*, 1751–1763.

(21) Hemmer, E.; Acosta-Mora, P.; Méndez-Ramos, J.; Fischer, S. Optical Nanoprobes for Biomedical Applications: Shining a Light on Upconverting and Near-Infrared Emitting Nanoparticles for Imaging, Thermal Sensing, and Photodynamic Therapy. *J. Mater. Chem. B* **2017**, *5*, 4365–4392.

(22) Tong, L.; Li, X.; Zhang, J.; Xu, S.; Sun, J.; Zheng, H.; Zhang, Y.; Zhang, X.; Hua, R.; Xia, H.; Chen, B. $NaYF_4:Sm^{3+}/Yb^{3+}@NaYF_4:Er^{3+}/Yb^{3+}$ Core-Shell Structured Nanocalorifier with Optical Temperature Probe. *Opt. Express* **2017**, *25*, 16047.

(23) Chu, M.; Shao, Y.; Peng, J.; Dai, X.; Li, H.; Wu, Q.; Shi, D. Near-infrared Laser Light Mediated Cancer Therapy by Photothermal Effect of Fe_3O_4 Magnetic Nanoparticles. *Biomaterials* **2013**, *34*, 4078-88.

(24) Shen, S.; Wang, S.; Zheng, R.; Zhu, X.; Jiang, X.; Fu, D.; Yang, W. Magnetic Nanoparticle Clusters for Photothermal Therapy with Near-Infrared Irradiation. *Biomaterials* **2015**, *39*, 67-74.

(25) Yang, D.; Yang, G.; Gai, S.; He, F.; An, G.; Dai, Y.; Lv, R.; Yang, P. Au_{25} Cluster Functionalized Metal–Organic Nanostructures for Magnetically Targeted Photodynamic/Photothermal Therapy Triggered by Single Wavelength 808 nm Near-Infrared Light. *Nanoscale* **2015**, *7*, 19568-19578.

(26) Chen, L.; Wu, L.; Liu, F.; Qi, X.; Ge, Y.; Shen, S. Azo-functionalized Fe_3O_4 Nanoparticles: a Near-Infrared Light Triggered Drug Delivery System for Combined Therapy of Cancer with Low Toxicity. *J. Mater. Chem. B* **2016**, *4*, 3660-3666.

(27) Shen, S.; Kong, F.; Guo, X.; Wu, L.; Shen, H.; Xie, M.; Wang, X.; Jin, Y.; Ge, Y. CMCTS Stabilized Fe_3O_4 Particles with Extremely Low Toxicity as Highly Efficient Near-Infrared Photothermal Agents for in vivo Tumor Ablation. *Nanoscale* **2013**, *5*, 8056-8066.

(28) Kim, J.; Lee, J. E.; Lee, S. H.; Yu, J. H.; Lee, J. H.; Park; T. G.; Hyeon, T. Designed Fabrication of a Multifunctional Polymer Nanomedical Platform for Simultaneous Cancer-Targeted Imaging and Magnetically Guided Drug Delivery. *Adv. Mater.* **2008**, *20*, 478–483.

(29) Sadat, M. E.; Kaveh Baghbador, M.; Dunn, A. W.; Wagner, H. P.; Ewing, R. C.; Zhang, J.; Xu, H.; Pauletti, G. M.; Mast, D. B.; Shi. D. Photoluminescence and Photothermal Effect of Fe_3O_4 Nanoparticles for Medical Imaging and Therapy. *Appl. Phys. Lett.* **2014**, *105*, 91903.

(30) Zhao, Y.; Sadat, M. E.; Dunn, A.; Xu, H.; Chen, C. H.; Nakasuga, W.; Ewing R. C.; Shi, D. Photothermal Effect on Fe_3O_4 Nanoparticles Irradiated by White-Light for Energy-Efficient Window Applications. *Sol. Energy Mater. Sol. Cells* **2017**, *161*, 247–254.

(31) Sickafus, K. E.; Wills, J. M.; Grimes, N. W. Cation Disorder and Vacancy Distribution in Nonstoichiometric Magnesium Aluminate Spinel, $MgO{\cdot}xAl_2O_3$ *J. Am. Ceram. Soc.* **2004**, *82*, 3279–3292.

(32) Liu, X.; Liu, J.; Zhang, S.; Nan, Z.; Shi, Q. Structural, Magnetic, and Thermodynamic Evolutions of Zn-Doped Fe_3O_4 Nanoparticles Synthesized Using a One-Step Solvothermal Method. *J. Phys. Chem. C* **2016**, *120*, 1328-1341.

(33) Rivero, M.; del Campo, A.; Mayoral, A.; Mazario, E.; Sanchez-Marcos, J.; Munoz-Bonilla, A. Synthesis and Structural Characterization of $Zn_xFe_{3-x}O_4$ Ferrite Nanoparticles Obtained by an Electrochemical Method. *RSC Adv.* **2016**, *6*, 40067–40076.

(34) Mazario, E.; Morales, M. P.; Galindo, R.; Herrasti, P.; Menendez, N. Influence of the Temperature in the Electrochemical Synthesis of Cobalt Ferrites Nanoparticles. *J. Alloys Compd.* **2012**, *536*, S222–S225.

(35) Mazur, M.; Barras, A.; Kuncser, V.; Galatanu, A.; Zaitzev, V.; Turcheniuk, K. V.; Woisel, P.; Lyskawa, J.; Laure, W.; Siriwardena, A. et al. Iron Oxide Magnetic Nanoparticles with Versatile Surface Functions Based on Dopamine Anchors. *Nanoscale* **2013**, *5*, 2692.

(36) Rodríguez-Carvajal, J. Lab. Léon Brillouin (CEA-CNRS), CEA/Saclay, 91191 Gif sur Yvette Cedex, FRANCE.

(37) Mccusker, L. B.; Von Dreele, R. B.; Cox, D. E.; Louer, D.; Scardi, P. Rietveld Refinement Guidelines. *J. Appl. Cryst.* **1999**, *32*, 36–50.

(38) Byrne, J. M.; Coker, V. S.; Cespedes, E.; Wincott, P. L.; Vaughan, D. J.; Pattrick, R. A. D.; Van Der Laan, G.; Arenholz, E.; Tuna, F.; Bencsik, M. et al. Biosynthesis of Zinc Substituted Magnetite Nanoparticles with Enhanced Magnetic Properties. *Adv. Funct. Mater.* **2014**, *24*, 2518–2529.

(39) Goldmann, A. S.; Schödel, C.; Walther, A.; Yuan, J.; Loos; K.; Müller, A. H. E. Biomimetic Mussel Adhesive Inspired Clickable Anchors Applied to the Functionalization of Fe_3O_4 Nanoparticles. *Macromol. Rapid Commun.* **2010**, *31*, 1608–1615.

(40) Xu, C.; Xu, K.; Gu, H.; Zheng, R.; Liu, H.; Zhang, X.; Guo, Z.; Xu, B. Dopamine as a Robust Anchor to Immobilize Functional Molecules on the Iron Oxide Shell of Magnetic Nanoparticles. *J. Am. Chem. Soc.* **2004**, *126*, 9938–9939.

(41) Schramm, L. L. Colloid Stability, in Emulsions, Foams, and Suspensions: Fundamentals and Applications, Wiley-VCH, Weinheim, 2005.

(42) Roper, D. K.; Ahn, W.; Hoepfner, M. Microscale Heat Transfer Transduced by Surface Plasmon Resonant Gold Nanoparticles. *J. Phys. Chem. C* **2007**, *111*, 3636–3641.

(43) Yang, J.; Fan, L.; Xu, Y.; Xia, J. Iron Oxide Nanoparticles with Different Polymer Coatings for Photothermal Therapy. *J. Nanoparticle Res.* **2017**, *19*, 333.

(44) Akhavan, O.; Meidanchi, A.; Ghaderi, E.; Khoei, S. Zinc Ferrite Spinel-Graphene in Magneto-Photothermal Therapy of Cancer. *J. Mater. Chem. B* **2014**, *2*, 3306-3314.

(45) Tian, Q.; Hu, J.; Zhu, Y.; Zou, R.; Chen, Z.; Yang, S.; Li, R.; Su, Q.; Han, Y.; Liu, X. Sub-10 nm Fe_3O_4@$Cu_{2-x}S$ Core–Shell Nanoparticles for Dual-Modal Imaging and Photothermal Therapy. *J. Am. Chem. Soc.* **2013**, *135*, 8571–8577.

(46) Li, B.; Wang, Q.; Zou, R.; Liu, X.; Xu, K.; Li, W.; Hu, J. $Cu_{7.2}S_4$ Nanocrystals: a Novel Photothermal Agent with a 56.7% Photothermal Conversion Efficiency for Photothermal Therapy of Cancer Cells. *Nanoscale* **2014**, *6*, 3274-3282.

(47) Tian, Q.; Jiang, F.; Zou, R.; Liu, Q.; Chen, Z.; Zhu, M.; Yang, S.; Wang, J.; Wang, J.; Hu, J. Hydrophilic Cu9S5 Nanocrystals: A Photothermal Agent with a 25.7% Heat Conversion Efficiency for Photothermal Ablation of Cancer Cells in Vivo. *ACS Nano* **2011**, *5*, 9761–9771.

(48) Stockert, J. C.; Blázquez-Castro, A.; Cañete, M.; Horobin, R. W.; Villanueva, A. MTT Assay for Cell Viability: Intracellular Localization of the Formazan Product is in Lipid Droplets. *Acta Histochem.* **2012**, *114*, 785–796.

TOC graphics